MODELING OF HYDROTHERMAL FLUID CIRCULATION AS A TOOL FOR VOLCANIC HAZARD ASSESSMENT

A. P. Rinaldi[(a)], J. Vandemeulebrouck[(b)], M. Todesco[(a)]

(a) Istituto Nazionale di Geofisica e Vulcanologia
Sezione di Bologna
Bologna, 40133, Italy
e-mail: rinaldi@bo.ingv.it, todesco@bo.ingv.it
(b) Laboratoire de Geophysique Interne et Tectonophysique
Université de Savoie
Le Bourget du Lac Cedex, 73376, France
email: Jean.Vandemeulebrouck@univ-savoie.fr

ABSTRACT

Monitoring of geophysical and geochemical observables at the surface plays a main role in the understanding of—and the hazard evaluation of— active volcanoes. Measurable changes in these parameters should occur when a volcano approches eruptive conditions. Hydrothermal activity is commonly studied as an efficient carrier of signals from the magmatic system. As the magmatic system evolves, the amount, temperature, and composition of magmatic fluids that feed the hydrothermal system change, in turn affecting the parameters that are monitored at the surface. Modeling of hydrothermal circulation, as shown in the past, may cause measurable gravity changes and ground deformation. In this work, we extend our previous studies and increase the number of observable parameters to include gas temperature, the rate of diffuse degassing, the extent of the degassing area, and electrical conductivity. The possibility of nonmagmatic disturbance needs to be carefully addressed to ensure a proper estimate of volcanic hazard.

INTRODUCTION

Volcanic hazard assessment is a major challenge in all countries where large communities reside near active volcanoes. The safety of the population requires that at any time, an appropriate alert level is achieved as eruptive conditions approach. This task is particularly complicated when long repose times elapse between subsequent eruptive events, and the unrest can last for decades before the actual eruption takes place. In this case, the state of volcanic activity needs to be carefully monitored in order to detect signals related to magma movement toward the surface. The fluids that feed fumaroles and hot springs in active volcanoes are a fundamental resource available for volcanic surveillance. In a volcanic region, a fraction of discharged fluids generally derives from magma degassing. If the magmatic source changes in time, because of a new material supply in the magma chamber or other differentation processes, the volatiles could also change, affecting both the composition and flow rate of fluids at the surface. Observed changes are generally caused by a complex interaction between the magmatic system and hydrothermal fluid circulation. Several changes in monitored parameters may be associated with the hydrothermal system rather than with the degassing magma, and may occur as the fluids ascend through porous rock.

High temperatures and pore pressures acting on porous rock can be responsible for ground deformation (Bonafede, 1991; Todesco et al., 2004; Hurwitz et al., 2007; Hutnak et al., 2009; Rinaldi et al., 2009a). Hydrothermal fluids can also influence self-potential and electrical resistivity, since these quantities depend on fluid flow pattern, temperature, and phase saturation. Through measurements carried out in various volcanic regions, many authors have inferred the main features of fluid circulation in the underground (Zlotnicki and Nishida, 2003; Finizola et al., 2004; Aizawa et al., 2009; Revil et al., 2008). The distribution of liquid-dominated, two-phase, and gas-dominated regions also determines the subsurface distribution of the fluid density. Changes in relative size or in the position of these regions can produce measurable gravity signals (Todesco and Berrino, 2005). Other studies have inferred the effects of fluid circulation as a fault lubricant and as a trigger for low-frequency seismic events (Bianco et al., 2004). Results also indicate that the amplitude of the observed changes mostly depend on the supply rate of magmatic fluids (Todesco, 2009). However, the state and properties of the degassing magma are not the only source that generates and influences the observable signals. Recent results highlight the role of rock properties in controlling the evolution of the parameters measured at the surface (Rinaldi et al., 2009b).

Since magmatic and hydrothermal processes may cause similar effects, the interpretation of signals collected at the surface is not always unequivocally

constrained. A simultaneous analysis of different geophysical and geochemical observables is a sound approach for interpreting monitoring data and to infer a consistent conceptual model.
In this work, we extend our previous studies and increase the number of observable parameters to include gas temperature, the rate of diffuse degassing, and electrical conductivity. Following a well-established approach, we first simulate the evolution of the hydrothermal system and then compute the observables in a postprocessing calculation. The simulation of hydrothermal fluid circulation is based on a conceptual model previously developed for the Campi Flegrei (Chiodini et al., 2003; Todesco et al., 2004; Todesco and Berrino, 2005): the hydrothermal system is fed by fluids of magmatic origin and an unrest phase is simulated as a period of increased magmatic degassing. We quantify and compare the evolution of the considered observable parameters after a generic period of unrest. Note that we do not intend to reproduce the history of a particular system.

MODELING THE HYDROTHERMAL FLUID CIRCULATION

Hydrothermal fluid circulation is here simulated using the TOUGH2 code (Pruess et al., 1999), which is a multipurpose simulator describing the coupled flow of heat and multiphase and multicomponent fluids through a porous material.

In this paper, we consider water and carbon dioxide as fluid components. The 2-D computational domain is 10 km wide and 1.5 km deep (Figure 1), and discretized into 2,580 elements (radial dimensions from 25 to 3196 m and thickness from 5 to 25 m). Bottom and side boundaries are impervious and adiabatic. Atmospheric conditions are fixed along the upper boundary, which is open to heat and fluid flows. Figure 1 also show the properties of the porous medium used in the simulation, kept constant during the simulation. The shallow hydrothermal circulation is driven by the injection of a hot mixture of water and carbon dioxide. The inlet of hot fluids, placed at the bottom of the domain near the symmetry axis, is 150 m wide and discharges a mixture at a temperature of ~ 600 K.

As described in previous work (Chiodini et al., 2003; Todesco et al., 2004), this prolonged activity of the fluid source generates a wide two-phase plume, with a shallow single-phase gas region (Figure 2). The plume is characterized by high temperatures (contour in Figure 2) and is pressurized with respect to the hydrostatic gradient.

Initial conditions are obtained by simulating a long-lasting (thousands of years) injection of magmatic fluids. The prescribed flow rate at the inlet (1,000 tons/day of CO_2 and 2,400 tons/day of H_2O) reflects the data collected at the Campi Flegrei caldera and corresponds to a CO_2/H_2O molar ratio of 0.17 (Chiodini et al., 2003).

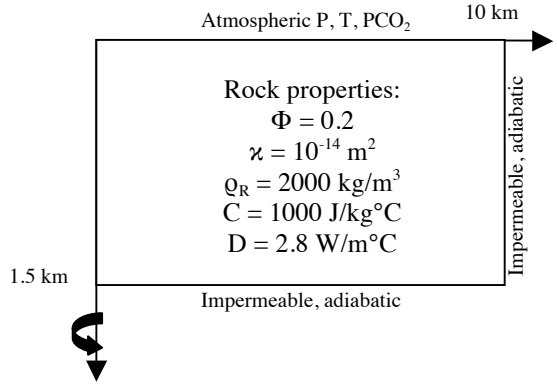

Figure 1. Computational domain and rock properties used in the hydrothermal fluid circulation. Fluid inlet is placed at the bottom near the symmetry axis. Symbols are: Φ porosity, κ permeability, ρ_R rock density, C rock specific heat, D rock thermal conductivity.

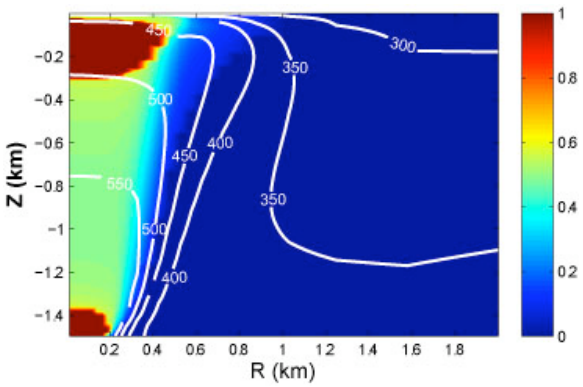

Figure 2. Gas volumetric fraction (color) and temperature distribution (contour) after the long-lasting injection of fluids. Two single phase gas zones are present in the domain (in red): near the inlet, and at shallow depth near the surface.

We are interested in the effects of a generic unrest to geophysical and geochemical observables. The unrest is simulated as a period (20 months) during which both the input of magmatic fluids and the CO_2 content increase (Table 1). The fluids are injected at the same, constant input entalphy, corresponding to a temperature of 600 K. The unrest period is followed by a longer quiet period (100 months), during which the mass flow rate at the inlet returns to the initial lower values.

Table 1. Inlet conditions during the unrest and the following quiet period. The enthalpy does not change during the simulation and corresponds to a temperature of ca. 600 K.

	CO_2 (ton/day)	H_2O (ton/day)	Molar ratio
Quiet	1000	2400	0.17
Unrest	6000	6100	0.40

The imposition of a larger discharge rate during the unrest is accompanied by pressure buildup and temperature changes. Also, the two-phase plume changes its shape and composition, owing to the different composition of injected fluids and the fact that pressure and temperature changes may enhance or reduce water evaporation. Detailed descriptions of the effect of the unrest on the two-phase plume can be found elsewhere (Rinaldi et al., 2009a, 2009b; Todesco, 2009; Todesco and Berrino, 2005; Todesco et al., 2003, 2004).

GEOPHYSICAL AND GEOCHEMICAL OBSERVABLES

As pointed out before, hydrothermal systems can generate a wide range of signals. Some observable parameters are directly related to fluid circulation and appear in the TOUGH2 output. Among these, we take into account in this work the amount and temperature of gas discharged at the surface. For other geophysical observables, a simple calculation is required. For example, it is possible to compute the compositional changes, considering the CO_2/H_2O molar ratio of the emitted gas. Such a calculation is made considering the average value of the molar ratio in the single-phase gas zone near the surface (Figure 2). Other observables can be derived from the TOUGH2 output, but require some postprocess calculation. Below, we present a background theory for electrical conductivity and gravity changes and ground displacement.

Background on Electrical Conductivity

Two main electrical conductivity mechanisms characterize the water-saturated porous medium. The first one is caused by the fluid flow inside the pore, through electromigration of anions and cations into the connected pore space. A second conduction mechanism occurs at the pore water-mineral interface, caused by a migration of the weakly adsorbed counterions (usually cations). We do not account for the effect of the electrical conductivity inside the grains, since measures performed on dry samples show very negligible values (Revil et al., 2002).

In this work, we follow the formulation of Revil et al. (1998) that takes into account the different behavior of different charge carriers: cations and the anions. This formulation is based on the "Hittorf transport numbers," which are the fraction of electrical current carried by the cations and anions in the free electrolyte. Similarly, it is possible to specify these numbers for surface conduction. Hittorf numbers are basically related to the ionic mobilities of the ions, and the electrical conductivity is given by combining the definitions of these numbers. Considering a solution with pH range 5–8, the counterions are mostly cations and the electrical conductivity is given by:

$$\sigma = \frac{\sigma_f}{F}\left[1 - t_{(+)} + F\xi + \frac{1}{2}(t_{(+)} - \xi) \left(1 - \frac{\xi}{t_{(+)}} + \sqrt{\left(1 - \frac{\xi}{t_{(+)}}\right)^2 + \frac{4F}{t_{(+)}}\xi} \right) \right] \quad (1)$$

where $F = \phi^{-m}$ is the electrical formation factor and represent the classical Archie's law, confirmed by several works; ϕ is the medium porosity; and m is the cementation exponent. Since the commonly observed range of the cementation factor in rock is $3/2 < m < 5/2$, it is a good approximation to set $m = 2$. σ_f is the electrical conductivity of the pore fluid (in Sm^{-1}); depending upon the salinity of the fluid. $t_{(+)}$ is the Hittorf number for the cation in the electrolyte and represents the electrical current carried by the cations (Revil et al., 1998). ξ is the ratio between the surface electrical conductivity (σ_S) observed at the water-mineral interface and the pore fluid electrical conductivity (σ_f), observed in the pores.

The surface electrical conductivity can be written as a function of the distribution of the charge density per unit pore volume Q_V (in Cm^{-3}) and of the ionic mobility of the cations $\beta_{(+)}^f$ (in $m^2s^{-1}V^{-1}$):

$$\xi = \frac{\sigma_S}{\sigma_f} \approx \frac{\beta_{(+)}^f \overline{Q}_V}{\sigma_f} \quad (2)$$

In the case of fluid with NaCl, the ionic mobility is $\beta_{(+)} = 5.19 \square 10 \square^8$ $m^2s^{-1}V^{-1}$ as shown by *Revil et al.* (1998). In the case of $\xi << 1$, as for high-salinity fluids, the electrical conductivity for a saturated porous medium can be approximated as follows:

$$\sigma = \frac{1}{F}\left(\sigma_f + \beta_{(+)}\overline{Q}_V\right) \quad (3)$$

Since there is no brine in our modeling of hydrothermal fluid circulation, we assume $\sigma_f = 0.1$ Sm^{-1}, to enhance the effect of the overall conductivity. This value is a good choice in the range of

pure water conductivity (0.01 Sm^{-1}) and water with high salinity (1 Sm^{-1}).

The above formulation is valid for a saturated medium, but hydrothermal areas are often characterized by the presence of two immiscible or two-phase fluids occupying the pore space of the medium. The case we develop below is valid for two-phase fluids: the liquid phase is the electrolyte wetting the mineral grains and the gas-phase is considered an insulating fluid. Considering the formulation for the saturated medium, the influence of the gas-phase upon electrical conductivity can be taken into account introducing the transformation proposed by Waxman and Smits (1968):

$$\begin{aligned} \phi^m &\rightarrow \phi^m S_w^n \\ \overline{Q}_V &\rightarrow \overline{Q}_V / S_w \end{aligned} \qquad (4)$$

where n is the saturation (or second) Archie exponent (generally $n = m$) and S_w is the pore volume space fraction occupied by liquid phase. A pore completely saturated in the liquid phase will have $S_w = 1$. Considering $m = n = 2$, the electrical conductivity as a function of the water saturation is given by:

$$\sigma = \phi^2 S_w^2 \left(\sigma_f + \beta_{(+)} \frac{\overline{Q}_V}{S_w} \right) \qquad (5)$$

The presence inside a pore of a gas phase (like water vapor or CO_2), considered nonwetting and insulating, will increase the electrical conductivity at the pore surface.

For a variety of rock types, there is a strong relationship (Jardani and Revil, 2009) between the charge density per unit pore volume (Q_V) and the permeability of the medium k, expressed in m^2:

$$\log_{10} \overline{Q}_V = -9.2 - 0.82 \cdot \log_{10} k \qquad (6)$$

A strong connection between these two parameters is valid since there exists a dependence of both on the specific surface area of the porous material.

Typically, as shown in several paper (Revil et al., 1998; Roberts, 2002; Vaughan et al., 1993), the electrolyte and surface conductivities are temperature dependent. From laboratory measurements (Revil et al., 1998), a linear temperature dependence is valid, both for the ionic mobility and for the brine conductivity:

$$\begin{aligned} \sigma_f &= \sigma_f(T_0)\left[1 + \alpha_f (T - T_0)\right] \\ \beta_{(+)} &= \beta_{(+)}(T_0)\left[1 + \alpha_{(+)} (T - T_0)\right] \end{aligned} \qquad (7)$$

where T_0 is the reference temperature (300 K), and the coefficients $\alpha_f \approx 0.023$ K^{-1}, and $\alpha_{(+)} \approx 0.037$ K^{-1} are temperature independent.

Gravity Changes and Ground Displacement

As pointed out by Todesco and Berrino (2005), changes in average fluid density generate a detectable gravity signal. The effect of a density changes on gravity is evaluated as a sum of the contribution of each gridblock of the computational domain. Todesco and Berrino (2005) calculate the vertical component of gravitational attraction on the surface at the symmetry axis as:

$$\Delta g_z = GV\Delta\rho_f \frac{z}{L^3} \qquad (8)$$

where G is the gravitational constant, V is the gridblock volume, $\Delta\rho_f$ its average fluid density, z its depth, $L^2 = r^2 + z^2$ its distance from the top of the symmetry axis, and r is the gridblock radius.

The vertical ground displacement is calculated using a mathematical model based on the linear theory of thermo-poro-elasticity and a system of distributed equivalent forces. (A full description of the displacement arising from hydrothermal circulation can be found elsewhere—Rinaldi et al., 2009a.) Each gridblock is considered as a potential source of deformation; then, the final displacement can be computed as a sum of the contribution of each element of the grid. Considering as observation point the symmetry axis at the surface, we have for each block:

$$u_z = \frac{1+\nu}{3\pi\mu} \Delta\theta V \frac{z}{R^3} \qquad (9)$$

where $\Delta\theta = \Delta p/H + \alpha_s \Delta T$ represents the dilatation (compression) of the grid element. V and z are the volume and depth of the element. R is the distance of the observation point from the element. We use the following mechanical properties: $1/H = 1/K - 1/K'_s$ is the Biot's constant (K = 5 GPa is the isothermal, drained bulk modulus and K'_s = 30 GPa is the bulk modulus of the solid constituent), μ = 2 GPa is the rigidity, ν = 0.25 is the Poisson's ratio, and $\alpha_s = 10^{-5}$ K^{-1} is the volumetric expansion coefficient.

Other approaches for ground deformation computing can be found elsewhere (Hurwitz et al., 2007; Hutnak et al., 2009; Todesco et al., 2004). In this work, we consider variation computed with respect to the initial steady-state condition.

RESULTING OBSERVABLES

In this section, temporal evolution and radial distribution of several observables deriving from the simulated hydrothermal fluid circulation will be analyzed.

Electrical Conductivity

We use Equation (5) to compute the electrical conductivity for each gridblock. The result is an electrical conductivity map over the entire domain, although a real measurement generally does not reach a depth of 1.5 km. Even if such a measurement were possible, the results are often biased, since a highly conductive layer (such as clay) may underestimate the conductivity in a deeper layer. However, we can evaluate the electrical conductivity effect deriving from changes in water saturation and temperature at depth.

Since we are interested in studying the effect of a disturbance, we calculate the electrical conductivity with respect to the initial steady-state value, rather than the absolute values. Figure 3 shows the electrical conductivity changes at the end of the unrest period (20 months of simulation).

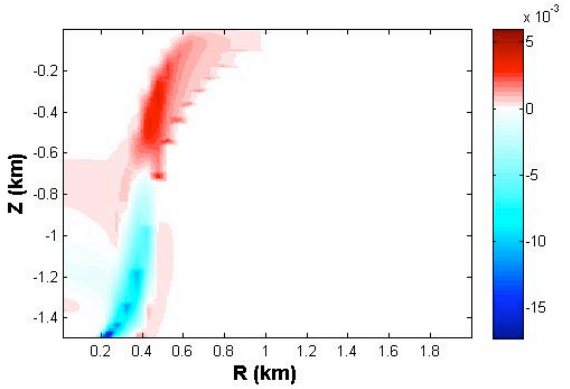

Figure 3. Changes in electrical conductivity (S/m) at the end of the unrest period (20 months).

The conductivity map presents some negative changes at depth (up to –0.015 S/m) near the inlet of magmatic fluids. Here, the gas phase, arising from the increased degassing, replaces the water-fluid phase. However, the temperature increases near the fluid source, beyond which there is also little increase in conductivity (0.001–0.002 S/m) at 400 m from the symmetry axis. The displaced fluids move toward the surface, after which we observe an increase in conductivity (up to 0.005 S/m) at shallower depth. Since most changes in temperature and water saturation happen at the border of the two-phase plume, electrical conductivity changes mainly at that location. Some minute changes occur inside the plume, which can explained by considering the small front of condensation (for positive changes) or evaporation (negative changes).

The electrical conductivity changes at the end of simulation are shown in Figure 4. Also, in this case the changes are mostly confined to the border of the plume; however, at the end of the simulation, the two-phase plume is larger, and we observe mainly negative changes (-0.005 S/m). Some positive variations (0.002 S/m) are still present at shallower depth, caused by fluids movements, and at depth near the inlet, where heating persists at the end of simulation.

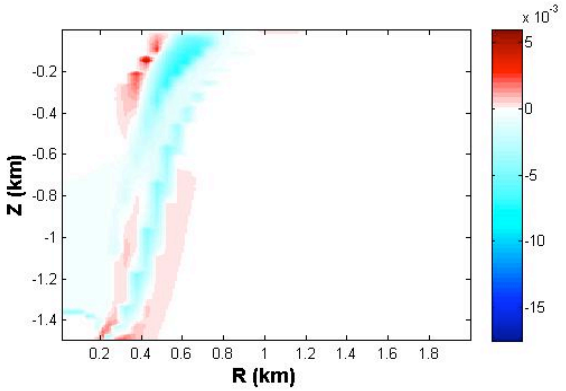

Figure 4. Changes in electrical conductivity (S/m) at the end of the simulation (120 months).

Temporal Changes

Analyzing the temporal trend of observable changes is essential for hazard evaluation. The temporal evolution of ground displacement, calculated at the surface on the symmetry axis, is shown in Figure 5 (line). Displacement presents an uplift at the beginning of the disturbance, as soon as the injection rate at the inlet is increased. Uplift reaches the maximum value (9 cm) at the end of the event. The quiet period is characterized by a slow subsidence that reflects the lower inflow of magmatic fluids at the inlet. The minimum ground elevation (-1 cm) is reached at the end of the simulation.

Figure 5 also shows the temporal evolution of the gravity changes caused by changes in average fluid density (dashed line). A positive trend characterizes the changes in gravity at the beginning of simulation, due to an increase in the average fluid density. The maximum value (40 μGal) is reached at the end of the unrest (20 months). As the simulation continues, the average fluid density declines, because the average gas fraction increases within the system. Then, gravity reaches a minimum value of -160 μGal at 80 months. Afterward, liquid water flows back toward the two-phase plume, after which the gravity changes begin again. When the simulation is over, a negative change of -100 μGal is still present.

The temporal evolution for the CO_2/H_2O molar ratio and the emission temperature of the discharged gases at the surface are shown in Figure 6. The ratio is calculated as an average value of the shallow single-phase gas zone. When the disturbance begins, the

molar ratio does not suddenly change, because the injected fluids spent some time before reaching shallower depth. The CO_2-rich fluids injected during the disturbance period reach the surface (and modify the gas composition observed) only after a characteristic time, which depends on the flow rate at the source, the system geometry, and the rock permeability (Todesco, 2009).

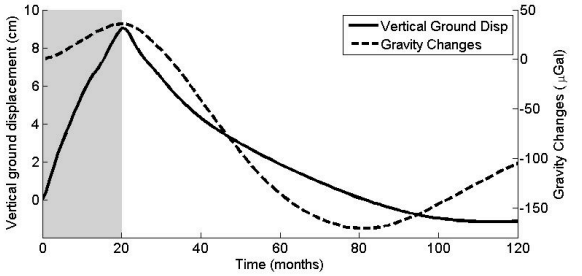

Figure 5. Temporal evolution of vertical ground displacement (line) and gravity changes (dashed line) at the symmetry axis. Shaded area represents the unrest period.

The CO_2/H_2O molar ratio (Figure 6, line) reaches its maximum value (0.33) after 32 months of simulation. Afterward, the CO_2 content declines again, reflecting lower enrichment during the quiet period. At the end of simulation, the molar ratio reaches a value lower than steady-state.

Changes in emission temperature of discharged gas are also associated with the disturbance, despite their very low magnitude. The temporal evolution (Figure 6, dashed line) shows two local maximum. The first one corresponds with fluid arrival at the surface; it occurs at the same time (32 months) as the CO_2/H_2O molar ratio maximum. A second maximum is attained at a later time (about 80 months), corresponding to an average heating of the system (see Rinaldi et al., 2009a).

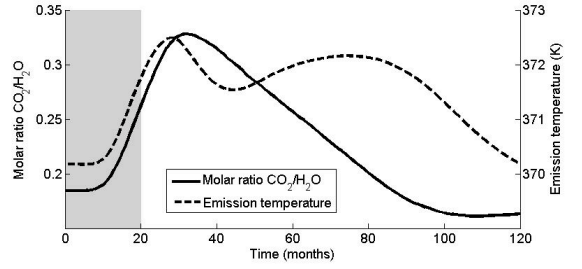

Figure 6. Temporal evolution of molar ratio CO_2/H_2O (line) and temperature of discharged gas (dashed line). Shaded area represents the disturbance period.

Radial Changes

Radial pattern are also important in the observables analysis, since it would be useful to infer the extent of degassing zones. The degassing area can be easily related to the amount of discharged gases at the surface, but radial patterns in gravity changes may also play a role.

Figure 7 shows the radial distribution of the discharged gases and the gravity changes. The figure is plotted at 32 months, which is when the CO_2/H_2O molar ratio reaches its maximum value. From the amount of gas (Figure 7, line) we infer that the degassing area is about 500–600 m from the symmetry axis. We note that the maximum amount of discharged fluids (4 kg/s) is very low if compared with the amount of fluids injected at the inlet during the disturbance (140 kg/s).

Gravity changes are related to density changes, then, since these occur mostly at the border of the two-phase plume, a maximum (or minimum) in gravity changes will arise at a radial distance corresponding to the surface extension of the plume. Figure 7 (dashed line) shows a maximum of 150 μGal at a distance of about 600–700 m from the symmetry axis, almost the same value we can infer from the total gas flow.

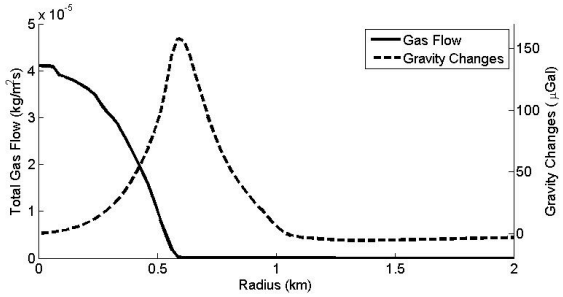

Figure 7. Radial distribution of gravity changes (dashed line) and amount of discharged gases at the surface (line) at t = 32 months, that is when the molar ratio CO_2/H_2O reaches its maximum (Fig. 6).

The same analysis can be done at the end of the simulation. The results are much the same, as shown in Figure 8. The magnitude of total gas flow is one-half that of the disturbance period (2 kg/s), and we observe a very strong variation in gravity changes: the minimum value is about -500 μGal, due to a large quantity of gas near the surface.

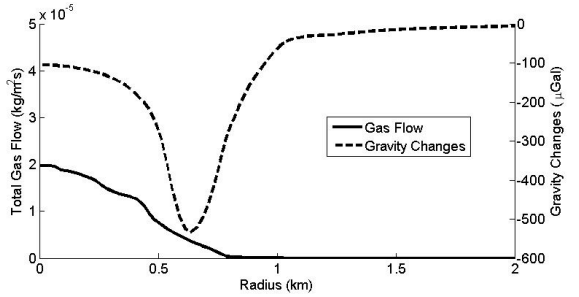

Figure 8. Radial distribution of gravity changes (dashed line) and amount of discharged gas at the surface (line) at the end of simulation (120 months).

Figure 9 shows the radial distribution of ground displacement calculated at different times. At the end of the disturbance (20 months, line in figure), the pattern of deformation looks like that of a Mogi-type, point source. The maximum uplift is right above the source and deformation vanishes within 4 km from the symmetry axis. A different pattern of deformation characterizes the subsidence. With time, changes in pressure and temperature become shallower along the border of the plume, then some spikes in displacement develop at 500-700 m from symmetry axis (Fig. 9, dashed line). At the end of simulation (Fig. 9, dot line), minor subsidence affects the axial region, and vertical displacement is mostly confined within 2 km from the symmetry axis.

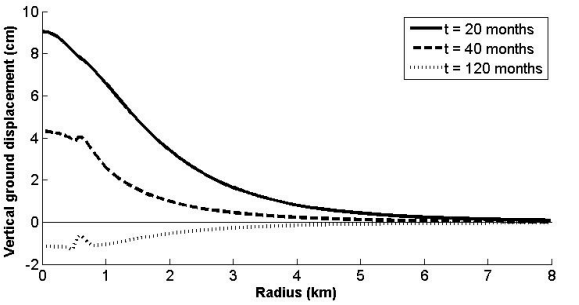

Figure 9. Radial distribution of vertical ground displacement at different time: 20 months (line), 40 months (dashed line) and 120 months (dot line).

CONCLUSION

Here we have presented an analysis of several geophysical and geochemical parameters. We have calculated the observables arising from changes in fluid circulation. The evolution of the hydrothermal system was simulated with the TOUGH2 numerical code (Pruess et al., 1999).

The evolution of the observables after a generic period of disturbance has been quantified and compared. Results show that increasing the fluid injection rate in our system (by a factor 3.5) results in measurable variations of surface signals.

The disturbance leads to a maximum uplift of the order of 10 cm, gravity changes up to 500 μGal and changes in electrical conductivity of the order of 10^{-2} Sm^{-1}. Changes in geochemical parameters were also observed, such as CO_2/H_2O molar ratio, total gas flow at the surface and emission temperature of the discharged gas.

The studied parameters do not show always the same temporal evolution. Ground displacement and gravity changes react suddenly at the higher injection of magmatic fluids at the inlet, after which we can easily discern when the disturbance is over. Other signals reach their maximum values after a characteristic time, depending on the flow rate at the source, the system geometry, and the rock permeability.

The evolution of the two-phase region over the entire simulation is associated with a complex pattern of variation along the surface, with peak values characterizing the edges of the plume. The extension of degassing area may subsequently be used as a benchmark for the measurements. Such an approch should emphasize the range of variations for several geophysical observables, such as electrical conductivity, gravity changes, and ground uplift.

An important result of this work is the analysis of the total gas flow through the ground surface. Although most of the observables present changes of the same order of magnitude as the observed variation, the values we found for the gas flow are underestimated compared to the measured changes in a real volcano, such as La Solfatara Volcano in the Campi Flegrei caldera (Italy). Such behavior may be explained by higher degassing at the bottom. However, the higher the fluid injection, the larger the observed signals at the surface. This difference in total gas flow may also mean that we are overestimating the gas dissolution in water, or that the gases may not redistribute in system in the same way we are simulating.

Although system properties and conditions strongly influence the calculated changes, our results support the importance of hydrothermal fluids in the surface changes of several geophysical and geochemical observables.

ACKNOWLEDGEMENT

The authors are grateful to A. Revil for helpful discussions. His comments greatly helped to improve this manuscript.

REFERENCES

Aizawa, K., Y. Ogawa, and T. Ishido, Groundwater flow and hydrothermal systems within volcanic edifices: Delineation by electric self-potential and magnetotellurics, *J. Geophys. Res.*, *114*(B01208), 2009.

Bianco, F., E. Del Pezzo, G. Saccorotti, and G. Ventura, The role of hydrothermal fluids in triggering the July August 2000 seismic swarm at Campi Flegrei, Italy: Evidence from seismological and mesostructural data, *J. Volcanol. Geotherm. Res., 133*, 229– 246, 2004.

Bonafede, M., Hot fluid migration: an efficient source of ground deformation: application to the 1982-1985 crisis at Campi Flegrei – Italy, *J. Volcanol. Geotherm. Res.*, *48*, 187-198, 1991.

Chiodini, G., M. Todesco, S. Caliro, C. Del Gaudio, G. Macedonio, and M. Russo, Magma degassing as a trigger of bradyseismic events: the case of Phlegrean Fields (Italy), *Geophys. Res. Lett.*, *30*(8), 1434-1437, 2003.

Finizola, A., A. Revil, E. Rizzo, S. Piscitelli, T. Ricci, J. Morin, B. Angeletti, L. Mocochain, and F. Sortino, Hydrogeological insights at Stromboli volcano (Italy) from geoelectrical, temperature and CO_2 soil degassing investigations, *Geophys. Res. Lett.*, *33*(L17304), 2006.

Hurwitz, S., L. B. Christiansen, and P. A. Hsieh, Hydrothermal fluid flow and deformation in large calderas: Inferences from numerical simulations, *J. Geophys. Res*, *112*(B02206), 2007.

Hutnak, M., S. Hurwitz, S. E. Ingebritsen and P. A. Hsieh, Numerical models of caldera deformation: Effects of multiphase and multicomponent hydrothermal fluid flow, *J. Geophys. Res.*, *114*(B04411), 2009.

Jardani, A., and A. Revil, Stochastic joint inversion of temperature and self-potential data, *Geophys. J. Int.*, 2009.

Pruess, K., C. Oldenburg, and G. Moridis, *TOUGH2 User's Guide, Version 2.0*, Report LBNL-43134, Lawrence Berkeley National Laboratory, Berkeley, Calif., 1999.

Revil, A., L. M. Cathles III, S. Losh, and J. A. Nunn, Electrical conductivity in shaly sands with geophysical application, *J. Geophys. Res..*, *103*(B10), 23925–23936, 1998.

Revil, A., D. Hermitte, E. Spangenberg, and J. J. Cochemé, Electrical properties of zeolitized volcaniclastic materials, *J. Geophys. Res.*, *107*(B8), 2002.

Revil, A., et al., Inner structure of La Fossa di Vulcano (Vulcano Island, southern Tyrrhenian Sea, Italy) revealed by high-resolution electric resistivity tomography coupled with self-potential, temperature, and CO_2 diffuse degassing measurements, *J. Geophys. Res.*, 113(B07207), 2008.

Rinaldi, A. P., M. Todesco, and M. Bonafede, Hydrothermal instability and ground displacement at the Campi Flegrei caldera, *Phys. Earth Planet. Int.*, 2009a.

Rinaldi, A. P., et al., Heterogeneous hydrothermal system, *in preparation*, 2009b.

Roberts, J. J., Electrical properties of microporus rock as a function of saturation and temperature, *J. App. Phys.*, *91*(3), 2002.

Todesco, M., Signals from the Campi Flegrei hydrothermal system: Role of a ''magmatic'' source of fluids, *J. Geophys. Res.*, *114*(B05201), 2009.

Todesco, M., and G. Berrino, Modeling hydrothermal fluid circulation and gravity signals at the Phlegraean Fields caldera, *Earth Planet. Sci. Lett.*, *240*, 328– 338, 2005.

Todesco, M., G. Chiodini, and G. Macedonio, Monitoring and modelling fluid emission at La Solfatara (Phlegrean Fields, Italy). An interdisciplinarity approach to the study of disffuse degassing, *J. Volcanol. Geotherm. Res.*, *125*, 57-79, 2003.

Todesco, M., J. Rutqvist, G. Chiodini, K. Pruess, and C. M. Oldenburg, Modeling of recent volcanic episodes at Phlegrean Fields (Italy): geochemical variations and ground deformations, *Geothermics*, *33*, 531-547, 2004.

Vaughan, P. J., K. S. Udell, and M. J. Wilt, The effects of steam injection on the electrical conductivity of an unconsolidated sand saturated with a salt solution, *J. Geophys. Res.*, *98*(B1), 509-518, 1993.

Waxman, M. H., and L. J. M. Smits, Electrical conductivities in oil-bearing shaly sands, *Soc. Pet. Eng. J.*, *8*, 107-122, 1968.

Zlotnicki, J., and Y. Nishida, Review on morphological insights of self-potential anomalies on volcanoes, *Surv. Geophys.*, *24*, 291–338, 2003.